AGU PUBLICATIONS

JGR

Journal of Geophysical Research: Atmospheres

RESEARCH ARTICLE
10.1002/2015JD023282

Key Points:
- Climatological aerosol optical depth (AOD) over the Red Sea is significant
- The climatological AOD shows a distinct seasonal and spatial pattern
- This manifests as asymmetric radiative surface cooling and atmospheric heating

Correspondence to:
H. Brindley,
h.brindley@imperial.ac.uk

Citation:
Brindley, H., S. Osipov, R. Bantges, A. Smirnov, J. Banks, R. Levy, P. Jish Prakash, and G. Stenchikov (2015), An assessment of the quality of aerosol retrievals over the Red Sea and evaluation of the climatological cloud-free dust direct radiative effect in the region, *J. Geophys. Res. Atmos.*, *120*, 10,862–10,878, doi:10.1002/2015JD023282.

Received 19 FEB 2015
Accepted 21 SEP 2015
Accepted article online 24 SEP 2015
Published online 20 OCT 2015

An assessment of the quality of aerosol retrievals over the Red Sea and evaluation of the climatological cloud-free dust direct radiative effect in the region

H. Brindley[1], S. Osipov[2], R. Bantges[1], A. Smirnov[3], J. Banks[4], R. Levy[5], P. Jish Prakash[2], and G. Stenchikov[2]

[1]Space and Atmospheric Physics Group, and NERC National Centre for Earth Observation, Imperial College London, London, UK, [2]Physical Science and Engineering, King Abdullah University of Science and Technology, Thuwal, Saudi Arabia, [3]Sigma Space Corporation, Lanham-Seabrook, Maryland, USA, [4]Space and Atmospheric Physics Group, Imperial College London, UK, [5]NASA-Goddard Space Flight Center, Greenbelt, Maryland, USA

Abstract Ground-based and satellite observations are used in conjunction with the Rapid Radiative Transfer Model (RRTM) to assess climatological aerosol loading and the associated cloud-free aerosol direct radiative effect (DRE) over the Red Sea. Aerosol optical depth (AOD) retrievals from the Moderate Resolution Imaging Spectroradiometer and Spinning Enhanced Visible and InfraRed Imager (SEVIRI) instruments are first evaluated via comparison with ship-based observations. Correlations are typically better than 0.9 with very small root-mean-square and bias differences. Calculations of the DRE along the ship cruises using RRTM also show good agreement with colocated estimates from the Geostationary Earth Radiation Budget instrument if the aerosol asymmetry parameter is adjusted to account for the presence of large particles. A monthly climatology of AOD over the Red Sea is then created from 5 years of SEVIRI retrievals. This shows enhanced aerosol loading and a distinct north to south gradient across the basin in the summer relative to the winter months. The climatology is used with RRTM to estimate the DRE at the top and bottom of the atmosphere and the atmospheric absorption due to dust aerosol. These climatological estimates indicate that although longwave effects can reach tens of $W\,m^{-2}$, shortwave cooling typically dominates the net radiative effect over the Sea, being particularly pronounced in the summer, reaching $120\,W\,m^{-2}$ at the surface. The spatial gradient in summertime AOD is reflected in the radiative effect at the surface and in associated differential heating by aerosol within the atmosphere above the Sea. This asymmetric effect is expected to exert a significant influence on the regional atmospheric and oceanic circulation.

1. Introduction

Quantifying the impact of aerosols on the Earth's climate has been recognized as one of the key challenges facing climate scientists today [*Intergovernmental Panel on Climate Change*, 2007, 2013]. Because of their typical size, natural aerosols such as mineral dust and sea salt dominate the tropospheric aerosol mass and are a key component of the Earth's environmental system. Dust aerosol in particular exerts strong radiative effects, interacting directly with both shortwave (SW) and longwave (LW) radiation [*Slingo et al.*, 2006; *Allan et al.*, 2011; *Ansell et al.*, 2014] and affecting cloud fields through its impact on atmospheric stability and hence convection [*Koren et al.*, 2005] and on cloud formation and microphysics [*Koehler et al.*, 2010; *Wurzler et al.*, 2000]. On short "weather" time scales these radiative effects have the potential to strongly influence the development of important phenomena such as African easterly waves and tropical cyclones [*Jury and Santiago*, 2010; *Evan et al.*, 2006]. Furthermore, they may stimulate significant dust-climate feedbacks by affecting the atmospheric circulation and precipitation patterns [*Miller et al.*, 2004], with consequences for soil moisture, vegetation cover and seasonality, and future dust production [*Nicholson*, 2000; *Woodward et al.*, 2005]. Dust uplift and long-range transport strongly modulates global biogeochemical cycles over land and ocean via associated nutrient transport and deposition [e.g., *Jickells et al.*, 2005] and mineral dust can also play a role in atmospheric chemistry [*de Reus et al.*, 2005].

While there have been a number of observational and modeling campaigns designed to probe dust-climate interactions over North Africa, the North Atlantic, Asia, the Americas, and the Mediterranean [e.g., *Tanré et al.*, 2003; *Reid and Maring*, 2003; *Huebert et al.*, 2003; *Heintzenberg*, 2009; *Haywood et al.*, 2011; *Washington et al.*, 2012], relatively little attention has been paid to the Arabian Peninsula and Red Sea. Qualitative observations

from the Total Ozone Mapping Spectrometer indicate that the Peninsula is home to a number of major dust sources, with background dust present throughout the year but activity peaking in the summer months [*Prospero et al.*, 2002]. Similarly, *Leon and Legrand* [2003] use 1 year of Meteosat data to identify dust activity in the vicinity of the northern Indian Ocean and highlight the Peninsula as home to one of the five major dust sources in the region. Simulations using a variety of dust emission scenarios and models also indicate that the region contributes a sizeable fraction to the global dust budget [e.g., *Zender et al.*, 2003; *Ginoux et al.,* 2001, 2012]. More locally, high-resolution modeling of a specific dust event has shown that dust presence can exert a marked impact on the surface energy balance of the Red Sea, with the dust induced cooling reaching up to 100 W m^{-2} [*Kalenderski et al.*, 2013]. In addition, while nutrient concentrations typically increase from north to south [*Wiekert*, 1987], Red Sea waters in general are highly nutrient deficient, becoming oligotrophic in the far north toward the Gulf of Aqaba [*Chase et al.*, 2011]. Deposition of wind-blown dust into the Sea can thus play a significant role in influencing nutrient cycles and productivity.

Although intermittent transported dust events might be expected to dominate the aerosol radiative effect when present over the Sea (observations off northwest Africa indicate localized dust effects in excess of 100 W m^{-2} [*Haywood et al.*, 2003]), the predominant background aerosol comprises sea salt particles which also interact directly and indirectly with the radiation field [*Carslaw et al.*, 2010]. Like dust, sea spray particle emissions are strongly wind speed dependent but also show a dependence on sea surface temperature [*O'Dowd and Smith*, 1993; *de Leeuw et al.*, 2011]. Previous estimates of their direct net radiative effect suggest a relatively small but highly variable impact of up to ~6 W m^{-2} at the top of the atmosphere (TOA) dependent on wind speed [e.g., *Satheesh and Moorthy*, 2005; *Ayash et al.*, 2008; *Yue and Liao*, 2012]. The Red Sea area, especially its northern part, is also a frequent recipient of anthropogenic aerosols that include biomass burning emissions from Africa and sulfates/nitrates from the Eastern Mediterranean [*Chen et al.*, 2008].

Because of the remoteness of the area, satellite retrievals provide a crucial tool for assessing aerosol loading over the Sea. However, agreement between aerosol properties inferred from measurements from different instruments, and even in some cases from the same measurements using different retrieval algorithms can be poor, particularly in the case of mineral dust [e.g., *Carboni et al.*, 2012]. Ground-based measurements which can be used to evaluate retrieval quality are thus highly desirable. Unfortunately, as indicated above, over the Arabian region such measurements are rather sparse. In this paper we take advantage of two sets of ship-based sun photometer observations gathered from a series of cruises which took place across the Red Sea during the autumn and winter of 2011, and through the winter and spring of 2013. To our knowledge, these data represent the first set of detailed aerosol measurements from the Red Sea since earlier scientific cruises within the Sea sampled conditions for, at most, up to a fortnight [*Tomasi and Prodi*, 1982; *Shifrin et al.*, 1985]. They thus provide a unique opportunity to assess the performance of satellite retrieval algorithms in this region across a range of different atmospheric aerosol loadings.

In the first part of this paper we introduce the ship-based measurements (section 2) and use them to evaluate the performance of colocated satellite retrievals from the Spinning Enhanced Visible and InfraRed Imager (SEVIRI) and the Moderate Resolution Imaging Spectroradiometer (MODIS) (section 3). While MODIS retrievals might be considered the "gold standard" over oceans and seas, the SEVIRI algorithm is somewhat simpler, being based on the standard method employed to derive aerosol optical depths and Ångström coefficients from the Advanced Very High Resolution Radiometer (AVHRR) [*Ignatov and Stowe*, 2002; *Brindley and Ignatov*, 2006]. In section 4 calculations of the cloud-free aerosol direct radiative effect along the ship track using the Rapid Radiative Transfer Model (RRTM) [*Mlawer et al.*, 1997] are compared with colocated measurements from the Geostationary Earth Radiation Budget (GERB) instrument [*Harries et al.*, 2005]. Having evaluated both the quality of the satellite retrievals and the ability of the model to capture the associated radiative effect, we use 5 years of SEVIRI day-time data to obtain a climatological picture of aerosol loading over the Red Sea. These data are then used to simulate the associated cloud-free aerosol direct radiative effect in order to assess the climatological aerosol impact on the radiative energy budget of the region (section 5). Conclusions to be drawn from the study are presented in section 6.

2. KAUST Ship Campaign Overview

With the ultimate aim of better quantifying the effect of aerosols on the Red Sea surface radiation fluxes, the first systematic ground-based aerosol measurements over the region were conducted between September

Table 1. Details of the R/V *Aegaeo* Cruise Leg Timings, Location, and Daily Mean Aerosol Optical Depth Range Recorded[a]

Cruise Leg	Observation Period	Observation Time (UTC)	Number of Days	Latitude	Daily Average AOD (675 nm)
Aegaeo_11_0 (0)	16/09/2011 to 09/10/2011	07:25–12:52	23	17–28 N	0.14–0.51
Aegaeo_11_1 (1)	16/10/2011 to 28/10/2011	07:20–13:23	13	20–25 N	0.14–0.35
Aegaeo_11_2 (2)	07/11/2011 to 17/11/2011	05:54–13:44	11	21–25 N	0.06–0.42
Aegaeo_11_3 (3)	22/11/2011 to 28/11/2011	06:37–12:36	7	22–23 N	0.07–0.23
Aegaeo_11_4 (4)	1/12/2011 to 11/12/2011	07:12–12:23	11	22–23 N	0.05–0.31
Aegaeo_13_0	28/02/2013 to 25/05/2013	05:47–12:18	59	21–28 N	0.11–0.96

[a]Number of days refers to the number of days on which measurements were actually taken during the cruise period. Cruise leg labels are consistent with those given on the NASA Maritime Aerosols Network.

and December 2011 on board the multipurpose Research Vessel (R/V) *Aegaeo*. Aerosol measurements were obtained from a hand-held sun photometer, following the protocol for the NASA Maritime aerosols network (MAN) measurements [*Smirnov et al.*, 2009]. Sixty-five measurement series from 16 September to 11 December 2011 were acquired during five different cruise legs. The number of observations taken and range of latitudes covered during each of the five legs are shown in Table 1 while Figure 1a maps the ship location, color coded for each leg. It is apparent both from this figure and Table 1 that leg 0 saw the ship sample the largest area of the Red Sea, while for several of the other cruise legs the ship was relatively stationary, acting more as a fixed observation point. Three sets of five-measurement series, each series typically lasting of the order 30 s, were taken each day and subsequently subjected to the MAN quality control and cloud-screening protocols described by *Smirnov et al.* [2009] to reach level 2. The estimated absolute uncertainty in individual level 2 observations does not exceed 0.02 in any of the spectral channels. The observation times given in Table 1 show the earliest and latest start times of each measurement series taken during each cruise leg. The daily average AOD range is that generated from level 2 daily mean values over the course of each leg.

To augment these data and sample a different set of meteorological conditions, a subsequent cruise by R/V *Aegaeo* was carried out during February to May 2013. Table 1 shows complementary information to that provided for the 2011 cruise for this case. Since the cruise began in the eastern Mediterranean the observation period given in Table 1 corresponds only to the part of the voyage over the Red Sea, the track of which is shown in Figure 1b. The data collected were subject to the same MAN protocols as those applied to the 2011 cruises. From Table 1 it is apparent that a greater range of aerosol optical depths was sampled in the 2013 cruise compared to those undertaken in 2011.

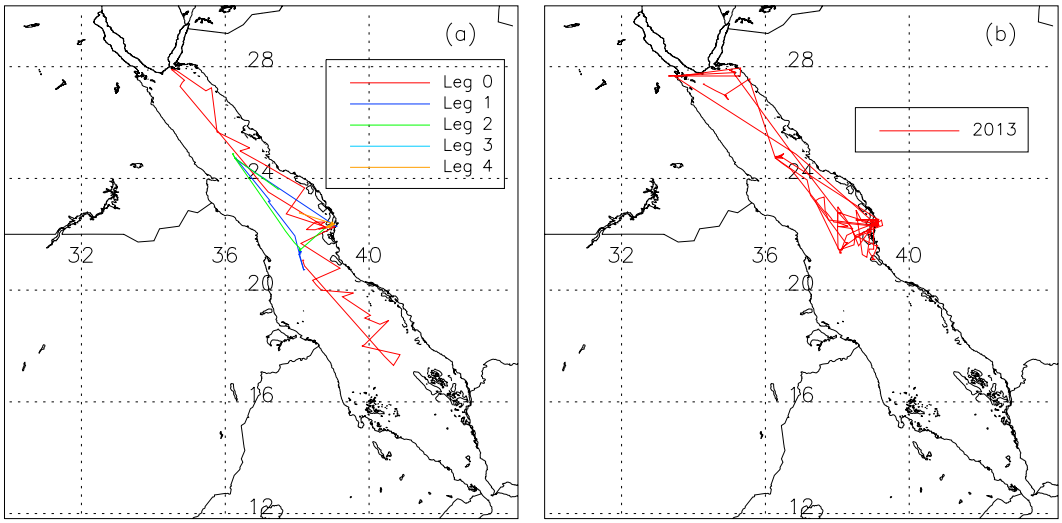

Figure 1. Location of R/V *Aegaeo* through (a) 2011 and (b) 2013 cruises.

3. Satellite Aerosol Products and Comparison With Ship-Based Observations

3.1. Satellite Products

We choose to use the ship-based observations to evaluate two satellite-based aerosol optical depth products. The first of these is the widely used dark target algorithm designed for use with MODIS, the core of which was developed by *Tanré et al.* [1997] but which was subsequently updated to include improved masking of clouds and ocean sediments and a special treatment for heavy dust outbreaks, including the retrieval of dust properties over sunglint [*Remer et al.*, 2005]. The algorithm is based on a look-up table (LUT) approach using precomputed spectral reflectance derived for a set of aerosol and surface parameters. The algorithm assumes that one fine and one coarse lognormal aerosol mode can be appropriately combined to represent the observed ambient aerosol properties. Spectral reflectance from the LUT is then compared with the equivalent MODIS-measured spectral reflectance to find the "best" (least squares) fit. Here we make use of collection 5.1 level 2 data, from both the *Terra* and the *Aqua* satellites, applying quality control criteria as directed by the MODIS team. The only change from the description of the algorithm provided by *Remer et al.* [2005] are some updates to the refractive indices used to create LUT spectral reflectance for certain of the coarse modes [*Levy et al.*, 2009]. Over ocean, the expected uncertainty in spectral optical depth, τ, is given as $\Delta\tau = \pm 0.03 \pm 0.05\tau$, nominally defined at a wavelength of 0.55 μm but shown to also hold for other spectral channels [*Remer et al.*, 2005]. However, it is acknowledged that nonspherical dust particles over ocean may result in larger errors in the retrieved τ values [*Levy et al.*, 2009].

Second, we consider optical depth retrievals derived from SEVIRI on Meteosat-9. Over ocean, optical depths at 0.63, 0.83, and 1.61 μm are obtained independently from the relevant channel reflectances using the relatively simple approach described by *Brindley and Ignatov* [2006]. In summary, this scheme involves the use of reflectance LUTs derived as a function of solar/viewing geometry and aerosol optical depth. For a given Sun-satellite geometry and spectral radiance that is either not flagged as cloudy using the scheme of *Ipe et al.* [2004] or classified as dusty [*Brindley and Russell*, 2006], the retrieved optical depth is that which minimizes the residual between the observed and simulated reflectance. In standard mode, one fixed semiempirical aerosol model is used in the construction of the LUTs, matching the representation originally employed in the retrieval scheme developed for AVHRR [*Ignatov and Stowe*, 2002]. This aerosol model was shown to give good agreement with Aerosol Robotic Network (AERONET)-measured optical depths for dust events observed off the west African coast, in the Persian Gulf, and over the Mediterranean Sea [*Brindley and Ignatov*, 2006; *Brindley and Russell*, 2008]. Using the optical depths derived from the different channels, one can also obtain estimates of Ångström coefficients: these can subsequently be used to scale the retrievals to alternative wavelengths as required. *De Paepe et al.* [2008] show that retrievals using this method exhibit root-mean-square (RMS) differences with colocated MODIS optical depths that are typically less than 0.1. For the purposes of this study retrievals are performed at a spatial resolution of 3×3 SEVIRI pixels, which is of the order 10 km^2 at nadir, ensuring broad consistency with the spatial scale of the L5.1 MODIS retrievals. It should be noted that SEVIRI retrievals are only carried out when the instrument solar and viewing zeniths are less than 70° and the scene is not affected by sunglint, here defined as a glint angle greater than 40°.

3.2. Intercomparison With R/V *Aegaeo* Measurements

To perform the satellite versus ship-based comparison, individual sun photometer measurements were first binned in 15 min intervals, retaining the overall mean and standard deviation of the points. In practice this means that at most three sets of ship-based observations are available per day, although the precise temporal sampling on a given day can change dependent on the start and end time of each measurement sequence (see Table 1). This strategy means that the binned observations can easily be matched to SEVIRI retrievals which are, in principle available at a 15 min temporal resolution during sunlit hours given the restrictions noted previously. Ship-based observations were then colocated with SEVIRI and MODIS by considering, in the first instance, all valid (cloud-free) satellite retrievals that occurred within a ± 1 h window and a 50 km radius of the ship location at the time of the measurement. While this matching criteria is relatively relaxed in the context of previous studies [e.g., *Brindley and Russell*, 2009; *Banks and Brindley*, 2013], it has the advantage of permitting the retention of a reasonable number of matches with MODIS overpasses from Terra and Aqua. Subsequent colocations were also performed using tighter matching criteria, and the impact assessed in the context of the SEVIRI retrievals.

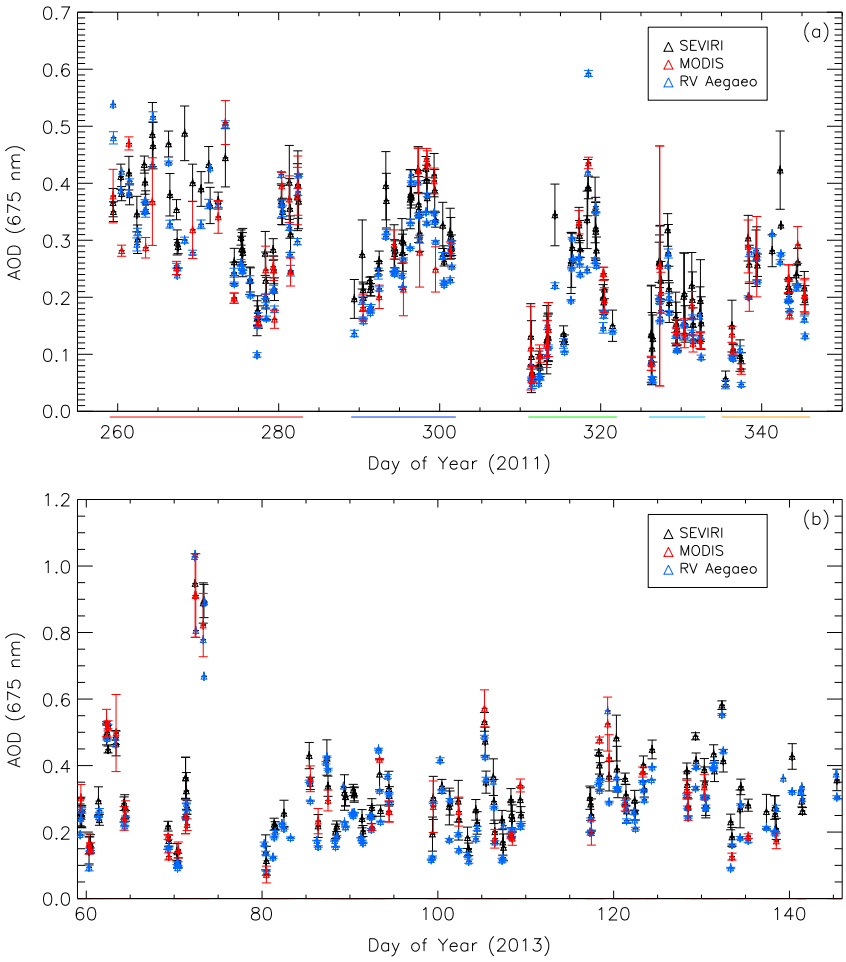

Figure 2. Aerosol optical depth (AOD) at 675 nm as a function of time as measured by the ship-based sun photometer (R/V *Aegaeo*) and as retrieved by MODIS and SEVIRI and colocated as described in the text. The vertical bars show the standard deviation in space and time over the course of each observational bin as seen in each measurement record: (a) 2011: the duration of each leg of the cruise is shown by the colored horizontal line with color coding as in Figure 1a; (b) 2013.

Figure 2a provides the time series of the sun photometer aerosol optical depths (AODs) at 675 nm, with, when available, the corresponding retrieved SEVIRI and MODIS values scaled to the same wavelength using the relevant Ångström coefficient [see *Brindley and Ignatov*, 2006]. Table 2 provides the corresponding statistics of the quality of the intercomparison for each leg individually and for the entire cruise, including only those points that have a valid AOD from the ship, SEVIRI, and MODIS. As might be anticipated from Figure 2a, in

Table 2. Comparison Statistics for SEVIRI, MODIS, and Ship-Based Sun Photometer AOD (at 675 nm) Observations, Including Pearson Correlation Coefficient (*R*), Root-Mean-Square (RMS) Difference and Bias (in the Sense SEVIRI-MODIS-Sun Photometer Observations)[a]

Cruise	No of Colocations	SEVIRI Ship *R*/RMS/Bias	MODIS Ship *R*/RMS/Bias	SEVIRI-MODIS *R*/RMS/Bias
2011 Leg 0	21	0.81/0.06/0.03	0.80/0.06/−0.01	0.85/0.06/0.03
2011 Leg 1	12	0.93/0.05/0.04	0.87/0.06/0.03	0.90/0.05/0.02
2011 Leg 2	13	0.93/0.06/0.01	0.93/0.06/0.02	0.98/0.02/−0.01
2011 Leg 3	12	0.84/0.06/0.05	0.79/0.04/0.02	0.92/0.04/0.03
2011 Leg 4	12	0.89/0.05/0.04	0.80/0.05/0.03	0.93/0.03/0.01
2011 All	70	0.91/0.06/0.03	0.89/0.06/0.01	0.93/0.04/0.02
2013	41	0.96/0.06/0.04	0.94/0.06/0.02	0.95/0.06/0.02

[a]Matching requirements were satellite observations within ±1 h and a 50 km radius around the ship location.

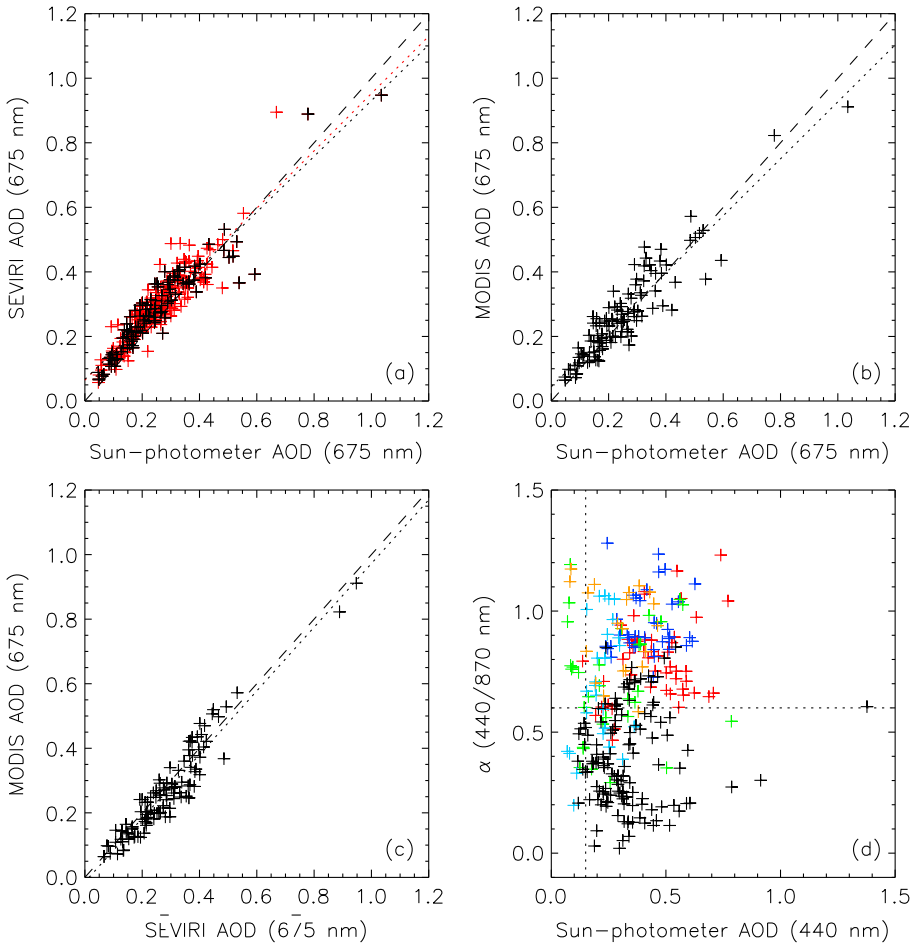

Figure 3. Scatterplots of (a) SEVIRI versus ship-based sun photometer AOD; (b) MODIS dark target versus ship-based sun photometer AOD; (c) MODIS versus SEVIRI AOD; (d) Ångström Coefficient, α, evaluated at 440 and 870 nm versus 440 nm AOD both from ship-based sun photometer. In Figures 3a–3c the black crosses are indicative of times when MODIS, SEVIRI, and sun photometer measurements were all available. Dashed lines indicate 1–1 agreement and dotted lines the linear least squares best fit between the instruments. Red points in Figure 3a show the extra measurements available when only SEVIRI and sun photometer observations are required to be present and the red dotted line is the associated linear least squares best fit. In Figure 3d the color coding matches that shown in Figure 1a in terms of 2011 cruise leg. The black crosses are 2013 data. Dotted lines show the criteria for dust and sea-salt aerosol suggested by *Dubovik et al.* [2002].

general, bearing in mind the relatively low number of matches, the agreement is rather good, with typical correlations of around 0.9 and RMS differences of 0.06. It is interesting to note that in general SEVIRI shows a higher correlation with the ship-based observations than MODIS, but that the bias, in the sense satellite minus ship, is also generally higher. The effect of attempting to compare a point-based measurement with that from a larger-scale satellite footprint may also be apparent in the improved level of agreement between MODIS and SEVIRI as opposed to that seen between satellite and ship-based observations.

Analogous information to that provided in Figure 2a is shown in Figure 2b for the 2013 cruise. Here R/V *Aegaeo* entered the Red Sea through the Suez Canal on 28 February, traversed the northeastern part of the basin and then performed more concentrated sampling to the northwest of Jeddah. The gaps in the record from 6–9 and 16–20 March, 5–8 and 20–26 April, and 5–7 and 22–24 May are indicative of actual breaks in the ship-based observational cycle and not prolonged cloudy conditions. When all three instruments agree that aerosol is present the level of agreement in the inferred values is very good, while RMS differences and biases are similar to those seen in the 2011 comparisons.

Figure 3 summarizes the information shown in Figure 2 and Table 2 in the form of scatter plots comparing the sun photometer AOD to SEVIRI (a) and MODIS (b), respectively. Here both 2011 and 2013 observations are

Table 3. Effect of Changing the Colocation Criteria on the Comparison Statistics Between SEVIRI and Sun Photometer 675 nm AOD[a]

Cruise Leg	No of Colocations	SEVIRI High *R*/RMS/Bias	SEVIRI Mid *R*/RMS/Bias	SEVIRI Low *R*/RMS/Bias
All	138	0.94/0.05/0.04	0.93/0.05/0.03	0.92/0.05/0.03
All	160	-	0.91/0.05/0.03	0.90/0.06/0.03
All	166	-	-	0.91/0.06/0.03

[a]Here "high" means that there must be a retrieval within ±15 min and a 10 km radius of the ship; "mid" requires a measurement within ±15 min but a 50 km radius; and low is the original within ±1 h and a 50 km radius choice. In the top row, at any given time there must be a retrieval using the high criteria for mid and "low" matches to be included in the comparison. In the middle row, at any given time there must be a retrieval using the mid criteria, and in the bottom row, there only needs to be a retrieval fulfilling the low criteria.

combined. Black points are illustrative of cases where retrievals were made from all three instruments. The red points in Figure 3a show the extra matches that were obtained between SEVIRI and the ship-based measurements. In both cases the dashed line shows the one-to-one agreement while the dotted lines show the linear least squares best fit between the two instruments. Again, the black dotted line in each case includes points when all three instruments provided a colocated retrieval while the red dotted line in Figure 3a includes the extra sun photometer/SEVIRI matches. In all cases the best fit *y* intercept has a small positive value, ranging from 0.04 for MODIS to 0.07 for SEVIRI (all points), the associated gradient having values of between 0.89 (SEVIRI) to 0.86 (SEVIRI, all points). For comparison, Figure 3c shows the scatter plot between MODIS and SEVIRI. Here as might be anticipated from Figures 3a and 3b, the *y* intercept of the linear least squares fit is very close to zero (< -0.01) and the gradient is 0.99.

To investigate the effect of the choice of matching criteria, in Table 3 correlations, biases, and RMS differences are presented for the ship-based observations versus SEVIRI for the entire 2011 cruise. Here we start from the criteria used originally (±1 h, within 50 km radius) and reduce these systematically. The results indicate that tightening the criteria marginally improves the correlation but that the effect is really rather minimal if there is a requirement that at least one observation meets the most stringent demands. Without this stipulation, relaxing the criteria has a more marked impact on the correlation but in all cases the RMS differences and biases are robust. It should also be noted that removing the requirement for a colocated MODIS overpass more than doubles the number of SEVIRI ship matches. However, the statistics are remarkably stable (compare Table 2 to Table 3), indicating that the SEVIRI retrievals and sun photometer measurements vary coherently with each other in space and time.

Finally, Figure 3d shows the Ångström coefficient, α, evaluated between 440 and 870 nm against 440 nm AOD, both derived from the sun photometer observations. For 2011 data the color coding matches that of Figure 1a while 2013 observations are shown in black. Previous authors have used this type of information to crudely diagnose aerosol type given its link to aerosol size. *Dubovik et al.* [2002] suggest that dust particles would be expected to exhibit a value of α of less than 0.6 (dotted horizontal line). Taken at face value, this would imply a large percentage of the observations from 2011 consist of smaller particles than might typically be associated with dust outbreaks. Conversely, the AOD values are rather higher than one would anticipate for oceanic aerosols, with a maximum value of 0.15 at 0.44 μm suggested by *Dubovik et al.* [2002] (vertical dotted line). From Figure 1 it is apparent that both ship campaigns primarily sampled the northern Red Sea. As previously noted, this area receives a significant amount of anthropogenic aerosol emissions including soot, sulfates, and nitrates. Trace anthropogenic elements associated with these emissions tend to have peak concentrations between August and October, consistent with the timings of the first two legs of the 2011 cruise [*Chen et al.*, 2008]. Hence, it is entirely possible that the aerosol measured during these legs is a complex mixture of natural (dust, sea salt) and anthropogenic components. In 2013 α values are typically smaller, falling below the nominal 0.6 "dust" criterion and indicative of a greater dominance of larger particles at this time.

4. Aerosol Radiative Effect During R/V *Aegaeo* Cruises

Having evaluated the quality of SEVIRI and MODIS retrievals, in this section we assess the associated cloud-free aerosol direct radiative effect (DRE) at the TOA using RRTM model simulations matched to the conditions seen along the 2011 and 2013 cruise tracks. The realism of the simulations is evaluated via comparison to the aerosol DRE derived from colocated GERB observations.

RRTM was configured to employ the 16 stream Discrete Ordinates setup to perform radiative transfer calculations in both the SW and the LW and as such, scattering effects are taken into account in both regimes. We define the simulated DRE as the difference between radiative fluxes calculated in perturbed (with aerosol) and control (without aerosol) runs, respectively. Note that the methods used to derive the corresponding observational estimates described below also attempt to isolate the aerosol only impact; hence we keep the same DRE nomenclature for ease of reference. In all cases we take the convention that a positive TOA DRE indicates a warming of the Earth-atmosphere system.

To calculate aerosol radiative characteristics, we assume that the particle size distribution can be represented by two lognormal distributions representative of coarse and fine modes. The median diameter and standard deviation of each of these distributions and their relative contributions to the total column AOD as a function of AOD were estimated from size distribution inversions obtained from selected AERONET sites across the Arabian Peninsula. The estimation process and resulting dependence of the distribution parameters on AOD is described in detail in *Osipov et al.* [2015]. The numbers of particles in each mode were scaled to match the retrieved SEVIRI AOD at each point along the ship track where a retrieval was available. Using these size distributions, and refractive indices representative of mineral dust internally mixed with 2.7% volume weighted hematite [*Balkanski et al.*, 2007], spectral optical properties of the aerosol in the shortwave were derived assuming a mixture of randomly orientated spheroids, following the approach of *Dubovik et al.* [2006]. In the longwave, given the reduced sensitivity to particle shape [e.g., *Osborne et al.*, 2011], optical properties were derived using Mie theory. The impact of haematite concentration on global estimates of dust DRE and on its diurnal cycle has been considered by *Balkanski et al.* [2007] and *Osipov et al.* [2015], respectively. In this paper the refractive index has been chosen so as to minimize the differences seen between the RRTM simulations and the observational estimates of TOA fluxes and DREs from GERB.

In order to perform the radiative transfer calculations the vertical profile of the aerosol also has to be specified. Here we use a representative profile for the Red Sea derived from vertically resolved measurements of 532 nm extinction from the Cloud-Aerosol Lidar with Orthogonal Polarization instrument onboard CALIPSO [*Winker et al.*, 2009]. We consider the period 2007–2013 and use the technique described in *Osipov et al.* [2015]. The resulting profile is normalized and used to generate layer by layer optical depths, constrained by the observed total AOD. Aerosol optical properties such as single-scattering albedo and phase function are assumed constant with height. To test the sensitivity of our simulated DREs to dust height and profile shape, for the 2011 and 2013 cruises we have performed a further set of calculations assuming a uniform vertical profile from the surface to 700 hPa. Our results (not shown) indicate that unsurprisingly, the largest effects of changing the dust profile are seen when the AOD is at its highest, and that for a given AOD the effect is larger in the LW than the SW. A similar finding regarding the relative magnitude of SW and LW clear-sky effects was reported by *Liao and Seinfeld* [1998]. We find that the maximum difference across both cruises in TOA LW DRE is 4.6 W m^{-2} while the corresponding maximum difference in the SW is less than 1.2 W m^{-2}. Over the cruises as a whole, the mean LW and SW differences are 1.5 and 0.2 W m^{-2}, respectively.

For SW surface boundary conditions we employ the ocean surface albedo parameterization from *Jin et al.* [2004]. This takes into account solar zenith angle, wind speed, the ratio of the incident direct and diffuse fluxes at the surface and chlorophyll concentration. Chlorophyll concentrations across the Red Sea are extracted from MODIS Aqua Level 3 global monthly mean Chlorophyll-A products while 10 m wind speeds are taken from European Centre for Medium Range Weather Forecasts Reanalyses (ERA-Interim) [*Dee et al.*, 2011]. In the LW, surface sea water emissivity from the Advanced Spaceborne Thermal Emission Reflection Radiometer spectral library is used [*Baldridge et al.*, 2009]. Surface temperatures and vertical profiles of temperature, water vapor, and ozone are prescribed from colocated ERA-Interim reanalyses. Minor gas concentrations (e.g., CO_2, CH_4, and N_2O) are taken from the relevant monthly climatology derived from the Global Modeling Initiative model [*Strahan et al.*, 2011].

GERB DREs are calculated using GERB-like high-resolution level 2 shortwave fluxes [*Dewitte et al.*, 2008] in conjunction with colocated SEVIRI AOD retrievals at their native wavelength of 630 nm. In the Edition 1 GERB processing, the conversion from broadband radiance to flux contains no explicit treatment for the effect of aerosol upon scene anisotropy. This can cause significant time-dependent errors in the flux fields, particularly over ocean because of the highly anisotropic nature of ocean surface reflectance. Typically, aerosols act to reduce this anisotropy; hence, there will be a systematic bias in the reflected SW flux as a function

of solar/view geometry if their impact is not taken into account when converting to flux from measured radiances. In this study aerosol effects on the SW radiance to flux conversion have been accounted for using the methodology described in *Brindley and Russell* [2008]. To derive SW DRE, SW fluxes are converted to albedo using a knowledge of the incident solar radiation. These albedos are then binned over solar zenith angle (θ_o) increments of 1° and linearly regressed against AOD. The *y* intercept for each bin is taken as the pristine-sky albedo at the given θ_o. The difference between an observed albedo and the relevant pristine-sky value is then multiplied by the appropriate incident SW flux to give the instantaneous SW DRE. This approach is analogous to that employed by *Loeb and Kato* [2002] when deriving direct aerosol effect estimates from Clouds and the Earth's Radiant Energy System observations.

GERB LW DREs are derived using the method developed by *Brindley* [2007] and *Brindley and Russell* [2009] for land scenes. The main aim of this approach is to obtain an estimate of the DRE which is measurement based but can isolate the aerosol effect: difficulty arises in the estimation of pristine-sky flux and its variation due to factors other than aerosol. As described in detail in these papers, for each individual pixel and time slot, cloud-free SEVIRI 10.8 μm brightness temperatures are used to identify the "most-pristine" day at that time and location over the previous 28 days. Once this day is identified for each location and time slot, the corresponding GERB LW flux is extracted and considered to represent "pristine" conditions. Clearly, one would expect a change in the LW flux if meteorological conditions alter between the identified pristine day and the days on which aerosol is present. Hence, for each time slot and location, "corrected" pristine-sky LW fluxes are calculated for days on which aerosol retrievals are actually attempted, accounting for the change in surface temperature and tropospheric humidity between the day of the observation and the originally identified pristine day. The temperatures and humidities are taken from colocated ERA-Interim data. Instantaneous LW DREs are then obtained by taking the difference between the observed GERB LW fluxes in the presence of aerosol and the corresponding corrected pristine-sky flux. The concept is based on the Infrared Dust Difference Index method developed by *Legrand et al.* [2001] when analyzing Meteosat observations.

Analysis of Figure 3d suggested that while the spring 2013 cruise sampled predominantly dusty conditions, the autumn/winter 2011 cruise saw more mixed aerosol. Hence, our choice of modeling the aerosol as purely dust through both cruises and for the climatological simulations described in section 5 needs justification. Recall that our focus in this and the following section is quantifying the aerosol cloud-free direct radiative effect. The aerosol DRE efficiency, DRE_{eff}, or the rate at which DRE increases with AOD, can be estimated from a linear fit of DRE against AOD. Purely observationally based estimates of DRE_{eff} were obtained using this approach from colocated sun photometer measurements of AOD and GERB DREs. The instantaneous DRE_{eff} obtained using all of the cruise measurements and for dusty observations only, as identified using the *Dubovik et al.* [2002] criteria (Figure 3d), were $67 \pm 6\,W\,m^{-2}$ (unit AOD)$^{-1}$ and $73 \pm 9\,W\,m^{-2}$ (unit AOD)$^{-1}$, respectively. Hence, both estimates overlap within their associated uncertainties. Moreover, the distributions of the AODs for both "mixed" and "dusty" points are very similar with mean (median) values changing by less than 0.02 (0.002). These results give us confidence that our decision to model the aerosol as purely dust is reasonable and will not significantly bias the results we obtain.

A comparison between the simulated (RRTM) and derived (GERB) SW DRE is shown in Figure 4a. The correlation between the DREs is 0.86 and a significant fraction (60%) of the RRTM TOA SW DRE estimates are within the GERB uncertainty range, estimated to be $15\,W\,m^{-2}$ [*Ansell et al.*, 2014]. However, there is a clear positive bias in computed reflected TOA fluxes compared to those observed by GERB (not shown) that is propagated through to the SW DRE estimates. Due to the relatively dark underlying surface, this bias is likely due to an overestimate in radiation backscattered from the nominal model aerosol layer. Increasing the aerosol asymmetry parameter by 15% for all wavelengths reduces this bias over the entire range of optical depths sampled through the campaign and the RMS flux error decreases from 10 to $4\,W\,m^{-2}$. In addition, all RRTM SW DRE values are now bounded by the GERB uncertainty range, with the RMS difference reduced from $15\,W\,m^{-2}$ to $5\,W\,m^{-2}$ (Figure 4a). Using this adjusted setup, both observations and model simulations agree that the TOA SW DRE ranges between approximately 0 and $-40\,W\,m^{-2}$ for the optical depths sampled during the ship cruises.

A possible physical reason for the apparent underestimate in asymmetry parameter could be the absence of large particles in our model size distribution. Measurements performed during the SAMUM 2006 and DODO campaigns [*Müller et al.*, 2010; *McConnell et al.*, 2008] indicate that coarse particles with radii bigger than 1 μm

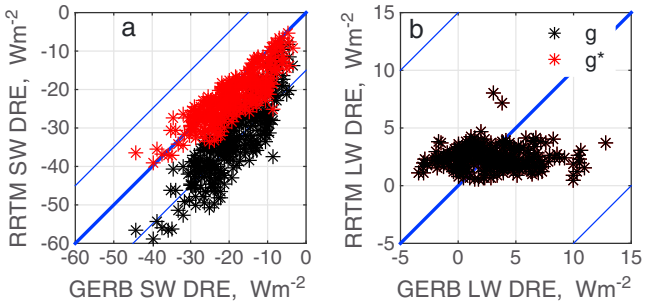

Figure 4. Scatterplots of RRTM and GERB TOA (a) SW DRE (W m^{-2}) and (b) LW DRE (W m^{-2}) as seen along 2011 and 2013 R/V *Aegaeo* cruises. Black stars correspond to calculations performed with the nominal dust optical characteristics described in the text. Red stars (g*) in Figure 4a indicate the results obtained with a manually increased asymmetry parameter value by 15% relative to the nominal setup. The thick solid lines correspond to "RRTM = GERB," and the thin solid lines to the uncertainty range that characterizes the estimated GERB error (± 15 W m^{-2}) in each case.

are not well captured by the AERONET retrieval algorithm. This is less sensitive to the supermicron particles because of the limited spectral range of AERONET sun photometers, between the ultraviolet and the beginning of the near IR [*O'Neill et al.*, 2008]. The presence of coarser particles would effectively increase the asymmetry parameter, consistent with the direction of the perturbation we have applied.

Figure 4b shows the corresponding LW DRE for the cruises as estimated from GERB and simulated by RRTM. In this case it is apparent from both satellite and simulated estimates that LW DREs tend to be much smaller than their SW counterparts. In addition, the RRTM estimates tend to be uniformly positive and small, at less than 5 W m^{-2}. In contrast, the GERB LW DREs can be both positive and negative and reach larger absolute values. However, the majority of values fall within the estimated uncertainty range on an instantaneous estimate of 15 W m^{-2} [*Ansell et al.*, 2014]. Moreover, the larger GERB LW DRE estimates that are present do not show a significant difference from their RRTM counterparts given their associated uncertainty.

5. Climatological Aerosol Loading and Direct Radiative Effect Over the Red Sea

The performance of the SEVIRI retrieval algorithm over the Red Sea shown earlier coupled with previous comparisons under a variety of conditions [e.g., *Brindley and Ignatov*, 2006; *De Paepe et al.*, 2008; *Haywood et al.*, 2011] gives confidence that, with the caveats discussed in section 3, the retrievals can be used to develop a longer term climatology of aerosol over the Sea. In particular, the temporal resolution of the retrievals can be exploited to identify events that polar-orbiting satellites may miss because of their sampling characteristics. However there is a further point to note here: the SEVIRI record itself is also subject to sampling biases, particularly in the morning (prior to ~ 0700 UTC) over the southern Red Sea in summer due to persistent glint conditions.

5.1. Mean Aerosol Optical Depth and Spatial Distribution

Bearing in mind these caveats, a survey of AOD at 630 nm over the Red Sea as derived from SEVIRI was carried out for the 5 years from 2008 to 2012, making use of all available observations each day between 0400 and 1430 UTC (0700–1730 LT). Figure 5 shows the time series of the monthly mean AOD derived over the entire Red Sea from all available time slots over the 5 year period. In creating this figure no attempt has been made to account for missing observations due to cloud or glint: effectively we are making the assumption that the aerosol loading stays constant at the mean observed level under these conditions. The seasonal variability exemplified in Figure 5a is consistent with expectations, with aerosol loading at its maximum during the summer months when dust activity in the region is at its most intense [*Prospero et al.*, 2002], typically peaking in July. The magnitude and variability seen in the mean AOD is also consistent with a longer-term record for the region derived from AVHRR (not shown). Figure 5b shows the number of SEVIRI observations that satisfied the criteria for an aerosol retrieval to be attempted during each month. The seasonality seen in the number of available observations is primarily a result of solar geometry. In particular, there is a systematic occurrence of sunglint conditions through May to August which particularly affects early morning (UTC) time slots. Finally, Figure 5c shows the monthly mean percentage of time that an aerosol retrieval was made given a valid radiance observation. This can be interpreted as a measure of the frequency of cloud presence over the sea as derived from SEVIRI, and, although noisy, suggests enhanced cloud occurrence during summer (June–August, JJA), associated with convection within the Intertropical Convergence Zone and southwesterly monsoon flow. A second peak is typically seen early

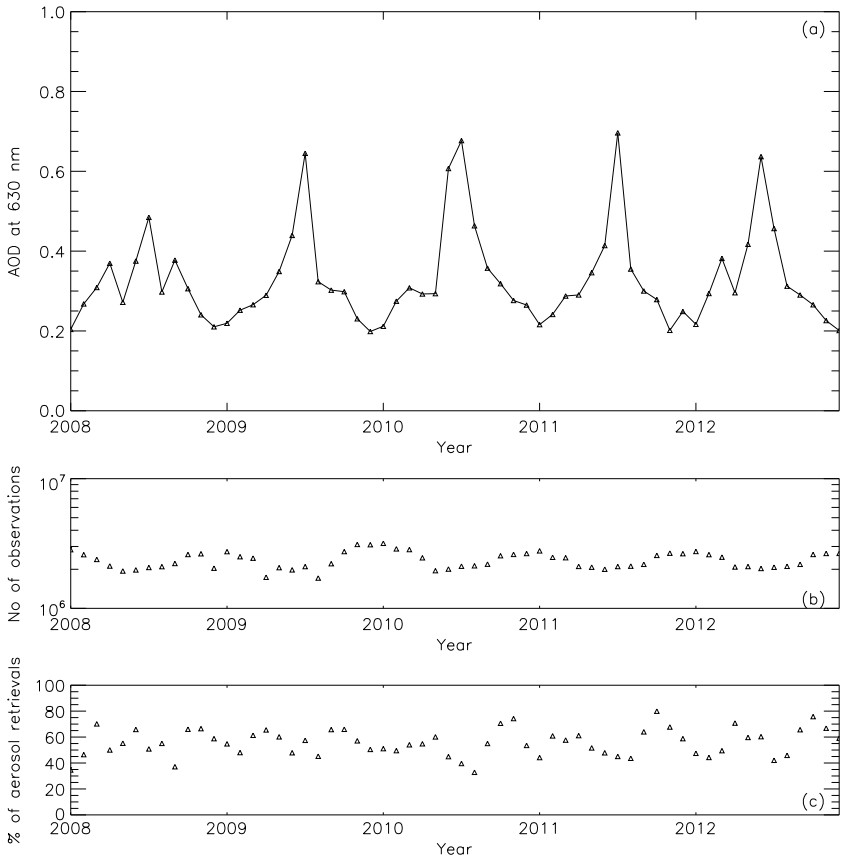

Figure 5. (a) Time series of monthly mean 630 nm AOD over the Red Sea derived from SEVIRI retrievals. (b) Number of observations for which an aerosol retrieval was attempted. (c) Percentage of the observations in Figure 5b that were classified as clear and inverted to obtain the mean AOD values shown in Figure 5a for each month.

in each year (JF), related to eastward propagating Mediterranean depressions and the Sudan heat low [*Fouda and Gerges*, 1994]. It should be noted that combining Figure 5b with Figure 5c implies that for all months over the 5 years in excess of ~700,000 retrievals contribute to the time series shown in Figure 5a. The systematic nature of the sunglint conditions does not appear to affect the seasonal pattern seen in the basin mean AODs as equivalent time series for early morning UTC time slots show essentially no difference in their seasonal behavior.

Decomposing the results spatially, Figures 6a and 6c show the 5 year monthly mean AOD pattern over the Red Sea for January and July, respectively. These are the months that show the lowest and highest basin mean AOD. The percentage of available observations that go into creating each mean is shown in Figures 6b and 6d. The impact of glint is already accounted for in these plots such that again, they effectively show the distribution of monthly mean cloud occurrence. Figures 6a and 6c reiterate the seasonal pattern shown in Figure 5a, higher AODs being seen across the whole of the basin in July compared to January. There is a distinct north/south divide, with a much larger seasonal enhancement seen over the southern part of the Sea (south of approximately 20°N) relative to the north. Comparing Figures 6b and 6d, there is also clearly a much more latitudinally stratified pattern in cloud occurrence in the July data relative to January, with a relatively low percentage of retrievals south of 20°N, particularly in the vicinity of the Eritrean coast. This stratified pattern has also been reported from an analysis of ground-based observations from coastal and island sites in the area over the summer months [*Hubert et al.*, 1983]. The relative lack of aerosol retrievals does mean that the assumption of consistent aerosol loading when clouds are present may be artificially inflating the mean AOD values shown over the southern part of the Sea in Figure 6d. However, the tendency for larger AOD values to be seen in the south (~1.2) relative to the north (~0.3) is again consistent with long-term patterns seen in AVHRR aerosol retrievals.

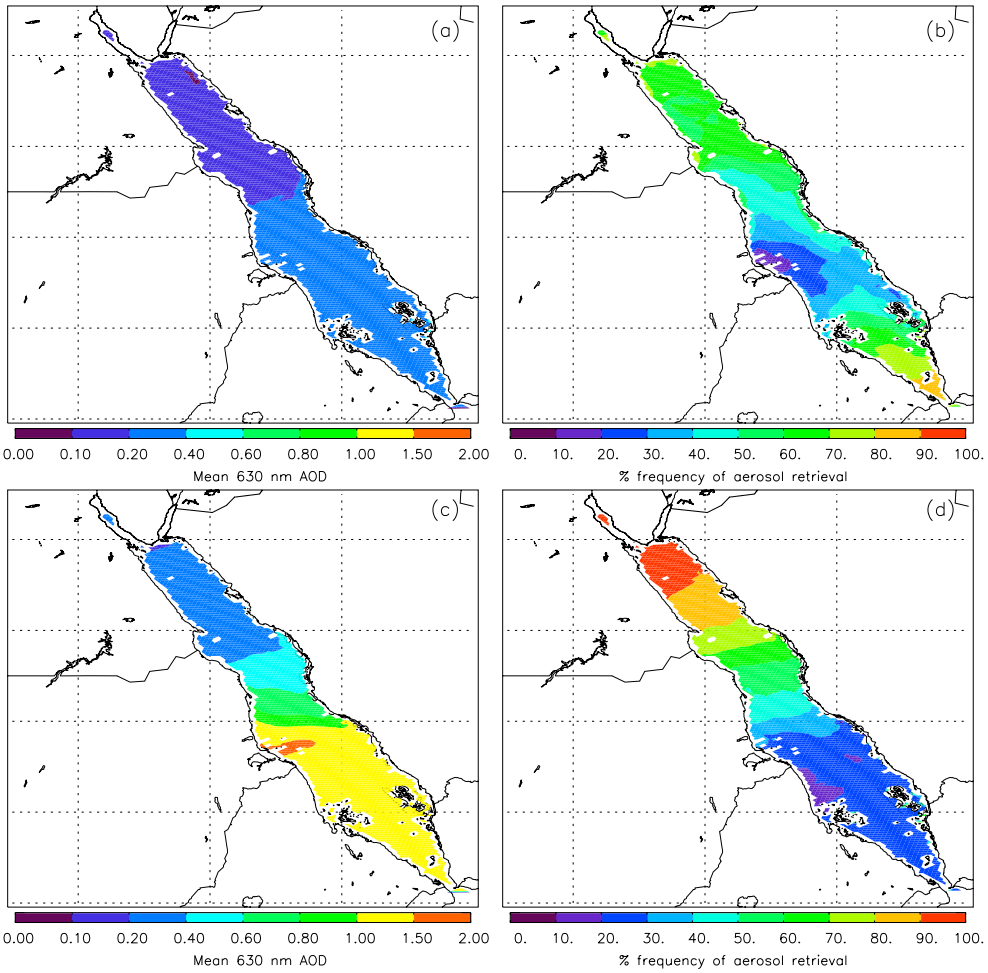

Figure 6. 2008–2012 monthly mean (a) 630 nm AOD and (b) percentage frequency of an aerosol retrieval for January from 2008 to 2012 over the Red Sea. (c, d) Equivalent information for July.

5.2. Aerosol Cloud-Free Direct Radiative Effect

In this section we assess the climatological radiative impact of aerosol over the Red Sea, making use of the AOD data described in section 5.1. Here we not only calculate the aerosol LW and SW DRE at the TOA but also at the bottom of the atmosphere (BOA). This provides insight into the contribution of aerosols to the overall surface energy balance of the region. By comparing the TOA and BOA effects, we can also obtain an estimate of the amount of radiation absorbed by aerosol, ΔF^A, over the full atmospheric column.

As a sanity check of our simulations we compare TOA DRE values to those obtained from GERB. Here it should be noted that while the GERB values are obtained by averaging instantaneous measurements across the 5 year period (2008–2012) to create daily means, the model results are generated using the 5 year climatological monthly mean aerosol optical depth. While the variation in solar geometry through a given month for a given time step over the study region is small, to capture the effect of its diurnal variation simulations are performed at an hourly resolution using diurnally varying solar geometry representative of the 15th day of each month. Within these simulations, meteorological fields are based on a diurnally resolved monthly mean climatology derived from 0.75° ERA-Interim fields over the corresponding 2008–2012 time period. Since there are consistent missing observation times in the GERB record (e.g., through the night), when forming the daily means shown in Figure 7, we make the assumption that the LW DRE during these times is equal to that when it is observed and that the SW DRE can be scaled by the number of available observation times to the total number of observations through the day. Hence, although we might expect broad consistency between the spatial patterns seen in the model simulations and observations an exact match would not be anticipated.

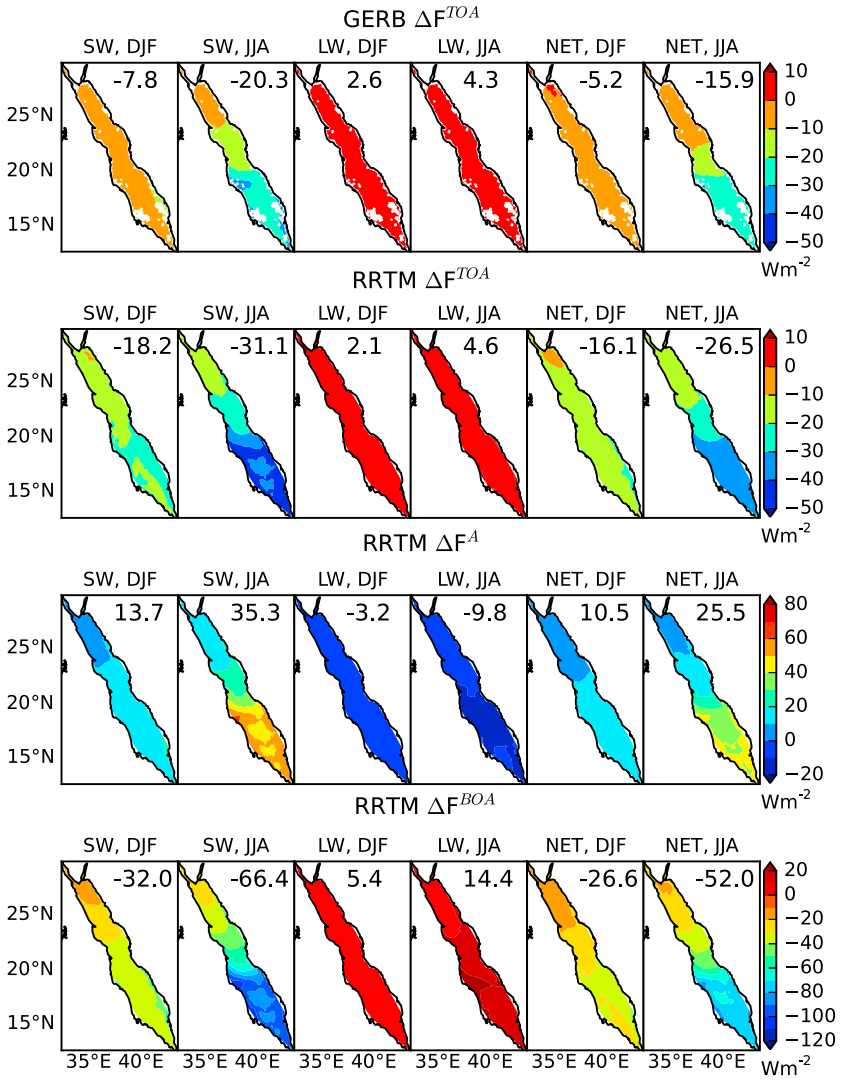

Figure 7. Daily mean TOA DREs from (first row) GERB and (second row) RRTM; (third row) ΔF^A from RRTM and (fourth row) BOA DREs from RRTM over the Red Sea in W m^{-2}. In each row the first two panels illustrate SW values, the middle two LW values, and the final two net values. In each pair of panels the left-hand panel is indicative of boreal winter (DJF), the right-hand panel, boreal summer (JJA). Basin mean values are provided within each panel. The RRTM calculations are performed using the climatological AODs derived from SEVIRI and include the manually increased asymmetry parameter discussed in section 4.

Figure 7 provides a summary of the radiative impact of aerosol over the Red Sea as diagnosed from RRTM (rows 2–4). For comparison the daily mean TOA DREs obtained from GERB are shown in the top row, subject to the caveats discussed above. Focusing on the TOA first, both observations and model simulations show that larger DREs are typically seen in summer consistent with the enhanced aerosol loading over this period (Figure 5a). The increased AOD gradient across the Red Sea in the summer months (Figure 6) is manifested as strong differential SW cooling across the basin, with the RRTM simulations indicating that the southern part has DREs that are of the order 30 W m^{-2} greater than those in the north. A similar differential pattern is seen in the corresponding GERB data, although the absolute SW DRE values tend to be systematically lower. This tendency is consistent with the results seen in Figure 4, even when the 15% increase in aerosol asymmetry parameter is applied. In summer the negative SW effect is much larger than the small positive LW values such that the net TOA DRE has a very similar pattern to the SW DRE in both GERB and RRTM data. In winter a more homogeneous pattern is seen in the SW, particularly in the GERB data. For RRTM, the LW effect is again dwarfed by the SW DRE such that the net values are practically identical to those in the SW and cooling occurs across the

basin. For GERB the picture is slightly different with LW DREs actually having a larger magnitude than those in the SW over the most northerly part of the basin. This results in a very small net warming of the Earth-atmosphere system in this region in this season.

Turning to the BOA (Figure 7, fourth row), here the RRTM simulations show a distinct north to south gradient in SW DRE for both winter and summer, although the magnitude of both the gradient and the actual effect is much larger in the latter season. SW cooling at the surface can reach up to 120 W m^{-2} in the southern part of the basin as opposed to ~25 W m^{-2} in the north during summer. In winter the corresponding figures are ~45 W m^{-2} and ~15 W m^{-2}, respectively. In the LW, the aerosol layer induces a warming at the surface through enhanced downward emission. In winter this does not exceed 10 W m^{-2} anywhere across the basin but in summer it can reach values in excess of 20 W m^{-2} and shows a north-south gradient whose pattern is similar to that seen in the corresponding SW DRE. The combination of the SW and LW behavior leads to a net BOA effect which is dominated by the SW component but whose overall degree of cooling is modulated by the heating effect of the aerosol in the LW.

We define atmospheric absorption due to aerosol, ΔF^A, as the difference between the TOA and BOA DREs. Hence, a positive value indicates additional atmospheric absorption and heating. The SW ΔF^A is predominantly determined by the aerosol single-scattering albedo and is always positive. Conversely, although smaller in magnitude, the LW ΔF^A tends to be negative, indicating that enhanced emission downward by the aerosol layer dominates over increased trapping of upwelling radiation: this behavior is strongly controlled by the atmospheric temperature profile. Figure 7 indicates that, as might be anticipated from the TOA and BOA DRE patterns, in winter net ΔF^A is relatively uniform across the sea, reaching a maximum value of 20 W m^{-2}. In summer, net ΔF^A is ~40–50 W m^{-2} larger over the southern compared to the northern Red Sea. In these simulations the values of net ΔF^A are dominated by the SW component such that aerosol always causes a radiative heating of the atmosphere.

6. Discussion and Conclusions

In this paper we have used a suite of modeling and observational tools to diagnose the climatological aerosol loading and its corresponding cloud-free direct radiative effect over the Red Sea. Comparisons of MODIS and SEVIRI retrievals of 675 nm AOD over the sea with ship-based measurements taken during two cruises in 2011 and 2013 indicate a good level of agreement between both the ship observations and individual satellite records and the two satellite records themselves. Correlations exceed 0.9 for both cruises with bias and root-mean-square (RMS) differences at or below 0.04 and 0.06, respectively. Both sets of satellite retrievals show a similar RMS difference with respect to the ship-based measurements but the SEVIRI retrievals tend to be biased slightly higher (by ~0.01) compared to those from MODIS. The sense of this difference is consistent with results reported by *De Paepe et al.* [2008] when considering the full geographical region viewed by SEVIRI but is smaller than the 0.07–0.09 values quoted in that work.

Investigations into the impact of the choice of matching criteria on the level of agreement between the ship measurements and SEVIRI-based retrievals showed that a marginal improvement in correlation and an associated reduction in bias and RMS differences could be achieved if tighter criteria were applied. More notable perhaps, the addition of the criterion that MODIS retrievals had to be available significantly reduced the available colocations without changing the quality of the intercomparison. In this study we use collection 5.1 MODIS aerosol retrievals in order to approximately match the spatial sampling of the SEVIRI aerosol retrievals (~9 × 9 km at nadir). However, it would be interesting in future to repeat the analysis with the relatively new collection 6 release [*Levy et al.*, 2013] which has the advantage of improved spatial resolution.

Given the performance of the SEVIRI retrievals over the range of conditions sampled through the ship cruises, we felt justified in deriving a 5 year monthly mean AOD record over the Red Sea covering the period 2008–2012. The rationale for using SEVIRI included both the sheer number of retrievals that were available because of the 15 min temporal sampling of the instrument, and the synergy that this provided with measurements of the components of the Earth's radiation budget taken by the GERB instrument. The derived climatology shows a distinct seasonality, with a clear peak in 630 nm AOD during the summer (JJA) and a corresponding minimum during the winter (DJF) months. Over the summer season the climatology indicates a marked spatial gradient in AOD, with highest values toward the south of the basin (typically

exceeding 1.0) and much lower values in the north (of the order 0.3). During the winter, although values in the southern part of the basin are still higher than those in the north, the gradient is much reduced. This pattern is consistent with that seen in other satellite retrievals and in climatologies created from surface visibility observations [*Hubert et al.*, 1983].

There are caveats associated with the climatology as created here. First, all available aerosol retrievals are used with no account taken for differences in the time of day of the retrievals from day to day: i.e., there is no attempt to create properly weighted daily mean AODs before monthly averaging is performed. This could artificially bias the record if the cloud detection algorithm used as a precursor to the retrieval itself systematically identifies more cloud at a particular time of day and aerosol AODs are also systematically biased one way or another at this time. There are known issues with the cloud detection algorithm used in the GERB processing resulting in artificially inflated cloud cover near the terminator, but these occur at higher solar zenith angles than at the 70° solar zenith angle cutoff employed in the SEVIRI aerosol retrievals. In addition, the cruise measurements considered in section 3 do not suggest any systematic AOD behavior with time over the Red Sea basin. More important perhaps is the assumption of constant AOD when the scene is classified as cloudy, particularly given that in the southern part of the basin in summer the percentage of retrievals can be as low as 20%. However, given that it is feasible for cloud and aerosol to coexist and that there are occasions when high aerosol loading can be artificially flagged as cloud [e.g., *Brindley and Russell*, 2006], this seems a sensible approach to have chosen.

Radiative transfer modeling using the climatological SEVIRI AOD as input illustrates that the spatial and seasonal variability in AOD summarized above translates to marked variability in the TOA cloud-free direct aerosol radiative effect (DRE) over the Red Sea. The sense of these modeling results are reinforced by observationally based estimates from GERB. Both model simulations and observations show that SW radiative cooling via enhanced reflection from the aerosol layer dominates over LW heating particularly during the summer months. While we note that an exact match should not be expected due to the different methods used to construct each estimate, the observations do show somewhat lower SW DREs than the simulations, with the converse being true for LW estimates. This change in behavior magnifies the differences seen between the observations and simulations in the net DRE. Nevertheless, we can be confident that for the Earth-atmosphere as a whole, the presence of aerosol causes a basin mean net cooling that is at least twice as large in the summer compared to the winter season.

At the surface the model simulations indicate a more dramatic aerosol DRE. Again, both the magnitude of the aerosol impact and its spatial distribution is significantly enhanced in summer relative to winter, with net DREs indicating a radiative cooling of up to 120 W m^{-2} in the southern part of the basin. Even on a basin mean, the net summer surface radiative cooling is of the order 66 W m^{-2}, approximately double the cooling seen in the winter. Similar to the TOA results the net effects are dominated by the SW component.

Putting the surface and TOA results together implies that overall aerosol acts to radiatively heat the atmosphere above the Sea. This effect is a manifestation of markedly enhanced absorption of SW radiation combined with a slight LW cooling due to enhanced emission to the surface by the aerosol layer. This net atmospheric heating is approximately 2.5 times as large in the summer (~25 W m^{-2}) compared to the winter months and again shows a much more pronounced north-to-south gradient across the basin during the former time period.

In summary our results indicate that the seasonal patterns in AOD and its spatial distribution are reflected in the TOA and surface direct radiative effects and thus also in the associated atmospheric radiative heating. Of particular interest is the strong spatial gradient seen in the climatological summertime AOD. This not only results in asymmetric effects at the surface but also associated differential radiative heating within the atmosphere above the Sea. Both would be expected to exert a significant influence on the regional atmospheric and oceanic circulation and will be the subject of further study using a coupled aerosol-atmosphere–ocean regional model.

Acknowledgments
The authors would like to thank Al Suwailem for help in organizing the routine aerosol ship observations at KAUST and De La Torre and Papadopoulos for help in conducting the first series of sun photometer observations. R/V *Aegaeo* was operated by the Hellenic Centre for Marine Research (HCMR), Greece, with the set of cruises described in this paper being organized by the King Abdullah University of Science and Technology (KAUST) in cooperation with the Woods Hole Oceanographic Institution, USA, under the auspices of the Red Sea exploration program. The research reported in this publication was principally supported by KAUST. In particular, for computer time, the resources of the KAUST Supercomputing Laboratory were used. Helen Brindley and Jamie Banks are partially supported by research grant KAUST CRG-1-2012-STE-IMP. Richard Bantges is supported by the UK National Centre for Earth Observation. The ship-based cruise data are available from the AERONET Maritime Aerosol Network at http://aeronet.gsfc.nasa.gov/new_web/maritime_aerosol_network.html. MODIS L5.1 data were obtained from the NASA GFSC Level 1 and Atmosphere Archive and Distribution System at http://ladsweb.nascom.nasa.gov/index.html. GERB data and SEVIRI AOD retrievals can be obtained from the British Atmospheric Data Centre (BADC) at http://catalogue.ceda.ac.uk/uuid/d8a5e58e59eb31620082dc4fd10158e2.

References

Allan, R., M. Woodage, S. Milton, M. Brooks, and J. Haywood (2011), Examination of long-wave bias in general circulation models over North Africa during May-July, *Q. J. R. Meteorol. Soc.*, *137*, 1179–1192.

Ansell, C., H. Brindley, Y. Pradhan, and R. Saunders (2014), Mineral dust aerosol net direct effect during GERBILS field campaign derived from SEVIRI and GERB, *J. Geophys. Res. Atmos.*, *119*, 4070–4086.

Ayash, T., S. Gong, and C. Jia (2008), Direct and indirect shortwave radiative effects of sea-salt aerosols, *J. Clim.*, *21*, 3207–3220.

Baldridge, A., S. Hook, C. Grove, and G. Rivera (2009), The ASTER spectral library version 2.0, *Remote Sens. Environ.*, *113*, 711–715.

Balkanski, Y., M. Schulz, T. Claquin, and S. Guibert (2007), Reevaluation of Mineral aerosol radiative forcings suggests a better agreement with satellite and AERONET data, *Atmos. Chem. Phys.*, *7*, 81–95.

Banks, J., and H. Brindley (2013), Evaluation of MSG-SEVIRI mineral dust retrieval products over North Africa and the Middle East, *Remote Sens. Environ.*, *128*, 58–73.
Brindley, H. (2007), Estimating the top-of-atmosphere longwave radiative forcing due to Saharan dust from satellite observations over a west African surface site, *Atmos. Sci. Lett.*, *8*, 74–79.
Brindley, H., and A. Ignatov (2006), Retrieval of mineral aerosol optical depth and size information from Meteosat second generation SEVIRI solar reflectance bands, *Remote Sens. Environ.*, *102*, 344–363.
Brindley, H., and J. Russell (2006), Improving GERB scene identification using SEVIRI: Infrared dust detection strategy, *Remote Sens. Environ.*, *104*, 426–446.
Brindley, H., and J. Russell (2008), Assessing the errors in shortwave radiative fluxes inferred from the Geostationary Earth Radiation Budget (GERB) instrument in the presence of dust aerosol, *J. Appl. Meteorol.*, *47*, 1659–1680.
Brindley, H., and J. Russell (2009), An assessment of Saharan dust loading and the corresponding cloud-free longwave direct radiative effect from geostationary satellite observations, *J. Geophys. Res.*, *114*, D23201, doi:10.1029/2008JD011635.
Carboni, E., et al. (2012), Desert dust satellite retrieval intercomparison, *Atmos. Meas. Tech.*, *5*, 1973–2002.
Carslaw, K., O. Boucher, D. Spracklen, G. Mann, J. Rae, S. Woodward, and M. Kulmala (2010), A review of natural aerosol interactions and feedbacks within the Earth system, *Atmos. Chem. Phys.*, *10*, 1701–1737.
Chase, Z., A. Paytan, A. Beck, D. Biller, K. Bruland, C. Measures, and S. Sanudo-Wilhelmy (2011), Evaluating the impact of atmospheric deposition on dissolved trace-metals in the Gulf of Aqaba, Red Sea, *Mar. Chem.*, *126*, 256–268.
Chen, Y., A. Paytan, Z. Chase, C. Measures, A. Beck, S. Sanudo-Wihelmy and A. Post (2008), Sources and fluxes of atmospheric trace elements to the Gulf of Aqaba, Red Sea, *J. Geophys. Res.*, *113*, D05306, doi:10.1029/2007JD009110.
de Leeuw, G., E. Andreas, M. Anguelova, C. Fairall, E. Lewis, C. O'Dowd, M. Schulz, and S. Schwartz (2011), Production flux of sea-spray aerosol, *Rev. Geophys.*, *49*, RG2001, doi:10.1029/2010RG000349.
De Paepe, B., A. Ignatov, S. Dewitte, and A. Ipe (2008), Aerosol retrieval over ocean from SEVIRI for the use in GERB Earth's radiation budget analysis, *Remote Sens. Environ.*, *112*, 2455–2468.
de Reus, M., H. Fischer, R. Sander, V. Gros, R. Kormann, G. Salisbury, R. Van Dingenen, J. Williams, M. Zollner, and J. Lelieveld (2005), Observations and model calculations of trace gas scavenging in a dense Saharan dust plume during MINATROC, *Atmos. Chem. Phys.*, *5*, 1787–1803.
Dee, D., et al. (2011), The ERA-Interim reanalysis: Configuration and performance of the data assimilation system, *Q. J. R. Meteorol. Soc.*, *137*, 553–597.
Dewitte, S., L. Gonzalez, N. Clerbaux, A. Ipe, C. Bertrand, and B. DePaepe (2008), The Geostationary Earth Radiation Budget Edition 1 data processing algorithms, *Adv. Space Res.*, *41*, 1906–1913, doi:10.1016/j.asr.2007.07.042.
Dubovik, O., B. Holben, T. Eck, A. Smirnov, Y. Kaufman, M. King, D. Tanré, and I. Slutsker (2002), Variability of absorption and optical properties of key aerosol types observed in worldwide locations, *J. Atmos. Sci.*, *59*, 590–608.
Dubovik, O., et al. (2006), Application of spheroid models to account for aerosol particle non-sphericity in remote sensing of desert dust, *J. Geophys. Res.*, *111*, D11208, doi:10.1029/2005JD006619.
Evan, A., J. Dunion, J. Foley, A. Heidinger, and C. Velden (2006), New evidence for a relationship between Atlantic tropical cyclone activity and African dust outbreaks, *Geophys. Res. Lett.*, *33*, L17701, doi:10.1029/2006GL026408.
Fouda, M., and M. Gerges (1994), Implications of climate change in the Red Sea and Gulf of Aden region: An overview, UNEP Regional Seas Reports and Studies No 156. [Available at http://www.unep.org/regionalseas/publications/reports/RSRS/pdfs/rsrs156.pdf.]
Ginoux, P., M. Chin, I. Tegen, J. Prospero, B. Holben, O. Dubovik, and S. Lin (2001), Sources and distributions of dust aerosols simulated with the GOCART model, *J. Geophys. Res.*, *106*, 20,255–20,273, doi:10.1029/2000JD000053.
Ginoux, P., J. Prospero, T. Gill, N. Hsu, and M. Zhao (2012), Global-scale attribution of anthropogenic and natural dust sources and their emission rates based on MODIS Deep Blue aerosol products, *Rev. Geophys.*, *50*, RG3005, doi:10.1029/2012RG000388.
Harries, J., et al. (2005), The Geostationary Earth Radiation Budget (GERB) project, *Bull. Am. Meteorol. Soc.*, *86*, 945–960.
Haywood, J., P. Francis, S. Osborne, M. Glew, N. Loeb, E. Highwood, D. Tanre, G. Myhre, P. Formenti, and E. Hirst (2003), Radiative properties and direct radiative effect of Saharan dust measured by the C-130 aircraft during SHADE: 1. Solar spectrum, *J. Geophys. Res.*, *108*, 8577, doi:10.1029/2002JD002687.
Haywood, J., et al. (2011), Motivation, rationale and key results from the GERBILS Saharan dust measurement campaign, *Q. J. R. Meteorol. Soc.*, *137*, 1106–1116, doi:10.1002/qj.797.
Heintzenberg, J. (2009), The SAMUM-1 experiment over southern Morocco: overview and introduction, *Tellus*, *61B*, 2–11.
Hubert, W., A. Hull, D. Morford, R. Englebretson (1983), Forecasters handbook for the Middle East/Arabian Sea. NAVENVPREDSCHFAC Contractor Report CR 83–06, Naval Environmental Prediction Research Facility, Monterey, CA, US. [Available at http://www.nrlmry.navy.mil/forecaster_handbooks/EastArabianSea/Forecasters%20Handbook%20for%20the%20Middle%20East-Arabian%20Sea.htm.]
Huebert, B., T. Bates, P. Russell, G. Shi, Y. Kim, K. Kawamura, G. Carmichael, and T. Nakajima (2003), An overview of ACE-Asia: Strategies for quantifying the relationships between Asian aerosols and their climatic impacts, *J. Geophys. Res.*, *108*(D23), 8633, doi:10.1029/2003JD003550.
Ignatov, A., and L. Stowe (2002), Aerosol retrievals from individual AVHRR channels. Part I: Retrieval algorithm and transition from Dave to 6S radiative transfer model, *J. Atmos. Sci.*, *59*, 313–334.
Intergovernmental Panel on Climate Change (IPCC) (2007), *Climate Change 2007: The Scientific Basis*, Cambridge Univ. Press, Cambridge, U. K.
Intergovernmental Panel on Climate Change (IPCC) (2013), *Climate Change 2013 : The Physical Science Basis*, Cambridge Univ. Press, Cambridge, U. K.
Ipe, A., C. Bertrand, N. Clerbaux, S. Dewitte, and L. Gonzalez (2004), Validation and homogenization of cloud optical depth and cloud fraction retrievals for GERB/SEVIRI scene identification using Meteosat-7 data, *Atmos. Res.*, *72*, 17–37.
Jickells, T., et al. (2005), Global iron connections between desert dust, ocean biogeochemistry, and climate, *Science*, *308*, 67–71, doi:10.1126/science.1105959.
Jin, Z., P. Charlock, L. Smith, and K. Rutledge (2004), A parameterization of ocean surface albedo, *Geophys. Res. Lett.*, *31*, L22301, doi:10.1029/2004GL021180.
Jury, M., and M. Santiago (2010), Composite analysis of dust impacts on African easterly waves in the Moderate Resolution Imaging Spectrometer era. *J. Geophys. Res.*, *115*, D16213, doi:10.1029/2009JD013612.
Kalenderski, S., G. Stenchikov, and C. Zhao (2013), Modeling a typical winter-time dust event over the Arabian Peninsula and the Red Sea, *Atoms. Chem. Phys.*, *13*, 1999–2014.
Koehler, K., S. Kreidenweiss, P. DeMott, M. Petters, A. Prenni, and O. Mohler (2010), Laboratory investigations of the impact of mineral dust aerosol on cold cloud formation, *Atmos. Chem. Phys.*, *10*, 11,955–11,968, doi:10.5194/acp-10-11955-2010.
Koren, I., Y. Kaufman, D. Rosenfeld, L. Remer, and Y. Rudich (2005), Aerosol invigoration and restructuring of Atlantic convective clouds. *Geophys. Res. Lett.*, *32*, L14828, doi:10.1029/2005GL023187.

Legrand, M., A. Plana-Fattori, and C. N'doumé (2001), Satellite detection of dust using the IR imagery of Meteosat: 1. Infrared difference dust index, *J. Geophys. Res.*, *106*, 18,251–18,274, doi:10.1029/2000JD900749.
Leon, J.-F., and M. Legrand (2003), Mineral dust sources in the surroundings of the north Indian Ocean, *Geophys. Res. Lett.*, *30*(6), 1309, doi:10.1029/2002GL016690.
Levy, R., L. Remer, D. Tanré, S. Mattoo, and Y. Kaufman (2009), Algorithm for remote sensing of tropospheric aerosol over dark targets from MODIS: Collections 005 and 051, Revision 2. [Available at http://modisatmos.gsfc.nasa.gov/MOD04_L2/atbd.html.]
Levy, R., S. Mattoo, L. Munchak, L. Remer, A. Sayer, F. Patadia, and N.-C. Hsu (2013), The Collection 6 MODIS aerosol products over land and ocean, *Atmos. Meas. Tech.*, *6*, 2989–3034, doi:10.5194/amt-6-2989-2013.
Liao, H., and J. Seinfeld (1998), Radiative forcing by mineral dust aerosols: Sensitivity to key variables, *J. Geophys. Res.*, *103*(D24), 31,637–31,645, doi:10.1029/1998JD200036.
Loeb, N., and S. Kato (2002), Top-of-atmosphere direct radiative effect of aerosols over the tropical oceans from the Clouds and the Earth's Radiant Energy System (CERES) satellite instrument, *J. Clim.*, *15*, 1474–1484.
McConnell, C., E. Highwood, H. Coe, P. Formenti, B. Anderson, S. Osborne, S. Nava, K. Desboeufs, G. Chen, and M. A. J. Harrison (2008), Seasonal variations of the physical and optical characteristics of Saharan dust: Results from the Dust Outflow and Deposition to the Ocean (DODO) experiment, *J. Geophys. Res.*, *113*, D00C03, doi:10.1029/2007JD009606.
Miller, R., I. Tegen, and J. Perlwitz (2004), Surface radiative forcing by soil dust aerosols and the hydrologic cycle, *J. Geophys. Res.*, *109*, D04203, doi:10.1029/2003JD004085.
Mlawer, E., S. Taubman, P. Brown, M. Iacono, and S. Clough (1997), Radiative transfer for inhomogeneous atmospheres: RRTM, a validated correlated-k model for the longwave, *J. Geophys. Res.*, *102*, 16,663–16,682, doi:10.1029/97JD00237.
Müller, D., et al. (2010), Mineral dust observed with AERONET Sun photometer, Raman lidar, and in situ instruments during SAMUM 2006: Shape-independent particle properties, *J. Geophys. Res.*, *115*, D07202, doi:10.1029/2009JD012520.
Nicholson, S. (2000), Land surface processes and Sahel climate, *Rev. Geophys.*, *38*, 117–1390, doi:10.1029/1999RG900014.
O'Dowd, C., and M. Smith (1993), Physiochemical properties of aerosols over the Northeast Atlantic—Evidence for wind-speed-related submicron sea-salt aerosol production, *J. Geophys. Res.*, *98*, 1137–1149, doi:10.1029/92JD02302.
O'Neill, N., T. Eck, J. Reid, A. Smirnov, and O. Pancrati (2008), Coarse mode optical information retrievable using ultraviolet to short-wave infrared Sun photometry: Application to United Arab Emirates Unified Aerosol Experiment data, *J. Geophys. Res.*, *113*, D05212, doi:10.1029/2007JD009052.
Osborne, S., A. Baran, B. Johnson, J. Haywood, E. Hesse, and S. Newman (2011), Short-wave and long-wave radiative properties of Saharan dust aerosol, *Q. J. R. Meteorol. Soc.*, *137*, 1149–1167.
Osipov, S., G. Stenchikov, H. Brindley, and J. Banks (2015), Diurnal cycle of the dust instantaneous direct radiative forcing over the Arabian Peninsula, *Atmos. Chem. Phys.*, *15*, 9537–9553, doi:10.5194/acp-15-9537-2015.
Prospero, J., P. Ginoux, O. Torres, S. Nicholson, and T. Gill (2002), Environmental characterisation of global sources of atmospheric soil dust identified with the Nimbus 7 Total Ozone Mapping Spectrometer (TOMS) absorbing aerosol product, *Rev. Geophys.*, *40*(1), 1002, doi:10.1029/2000RG000095.
Reid, J., and H. Maring (2003), Foreword to special section on the Puerto Rico Dust Experiment (PRIDE), *J. Geophys. Res.*, *108*(D19), 8585, doi:10.1029/2003JD003510.
Remer, L., et al. (2005), The MODIS aerosol algorithm, products, and validation, *J. Atmos. Sci.*, *62*, 947–973.
Satheesh, S., and K. Moorthy (2005), Radiative effects of natural aerosols: A review, *Atmos. Environ.*, *39*, 2089–2110.
Shifrin, K., V. Volgin, B. Volkov, O. Yershov, and A. Smirnov (1985), Optical depth of atmospheric aerosol over the sea, *Issled. Zemli Kosmosa*, *2*, 21–30, [Engl. Trans. Soviet Journal of Remote Sensing, 5(4), 591–605, 1989].
Slingo, A., et al. (2006), Observations of the impact of a major Saharan dust storm on the atmospheric radiation balance. *Geophys. Res. Lett.*, *33*, L24817, doi:10.1029/2006GL027869.
Smirnov, A., et al. (2009), Maritime Aerosol Network as a component of Aerosol Robotic Network, *J. Geophys. Res.*, *114*, D06204, doi:10.1029/2008JD011257.
Strahan, S., et al. (2011), Using transport diagnostics to understand chemistry climate model ozone simulations, *J. Geophys. Res.*, *116*, D17302, doi:10.1029/2010JD015360.
Tanré, D., et al. (1997), Remote sensing of aerosol properties over oceans using the MODIS/EOS spectral radiances, *J. Geophys. Res.*, *102*, 16,971–16,988, doi:10.1029/96JD03437.
Tanré, D., J. Haywood, J. Pelon, J. Leon, B. Chatenet, P. Formenti, P. Francis, P. Goloub, E. Highwood and G. Myhre (2003), Measurement and modeling of the Saharan dust radiative impact: Overview of the Saharan Dust Experiment (SHADE). *J. Geophys. Res.*, *108*(D18), 8574, doi:10.1029/2002JD003273.
Tomasi, C., and F. Prodi (1982), Measurements of atmospheric turbidity and vertical mass loading of particulate matter in marine environments (Red Sea, Indian Ocean and Somalian Coast), *J. Geophys. Res.*, *87*, 1279–1286, doi:10.1029/JC087iC02p01279.
Washington, R., et al. (2012), Fennec—The Saharan Climate System, *CLIVAR Exchange.*, *60*(17), 31–33.
Wiekert, H. (1987), Plankton and the pelagic environment, in *Red Sea*, edited by A. Edwards and S. Head, pp. 90–111, Pergamon Press, Oxford, U.K.
Winker, D., M. Vaughan, A. Omar, Y. Hu, K. Powell, Z. Liu, W. Hunt, and S. Young (2009), Overview of the CALIPSO mission and CALIOP data processing algorithms, *J. Atmos. Oceanic Technol.*, *26*, 2310–2323, doi:10.1175/2009JTECHA1281.1.
Woodward, S., D. Roberts, and R. Betts (2005), A simulation of climate change-induced desertification on mineral dust aerosol, *Geophys. Res. Lett.*, *32*, L18810, doi:10.1029/2005GL023482.
Wurzler, S., T. Resin, and Z. Levin (2000), Modification of mineral dust particles by cloud processing and subsequent effects on drop size distributions, *J. Geophys. Res.*, *105*, 4501–4512, doi:10.1029/1999JD900980.
Yue, X., and H. Liao (2012), Climatic responses to the shortwave and longwave direct radiative effects of sea salt aerosol in present day and the last glacial maximum, *Clim. Dyn.*, *39*, 3019–3040.
Zender, C., H. Bian, and D. Newman (2003), Mineral Dust Entrainment and deposition (DEAD) model: Description and 1990s dust climatology, *J. Goephys. Res.*, *108*(D14), 4416, doi:10.1029/2002JD002775.